A Novel Hybrid-Flux Dual-Mechanical-Port Dual-Electrical-Port Machine for Hybrid Electric Vehicles

Ziqi Huang, Mingyuan Jiang, Shuangxia Niu, *Senior Member*, *IEEE*, Zekai Lyu, Wenjie Wu, Longfei Xiao

***Abstract*—This paper presents a novel hybrid-flux dual-mechanical-port dual-electrical-port machine (DMP-DEPM) and its analytical model. The design features radial flux (RF) coils, and transverse flux (TF) coils that are spatially perpendicular to each other, thus reducing the interaction between the two sets of windings. The inner rotor connects to an internal combustion engine, serving as a mechanical input, while the outer rotor links to a gearbox, acting as a torque output. This dual-electrical-port configuration addresses the limitations of single-electrical-port transverse flux machines in hybrid electric vehicles, enabling simultaneous operation as a motor and generator. In motor mode, it offers higher torque density and efficiency than dual-rotor transverse flux machines. The paper outlines the design, operational principles, and an analytical model using the equivalent magnetic circuit method. Optimization and parameter selection are discussed, and finite-element analysis (FEA) is used to examine characteristics like flux density and back electromotive force (EMF). A prototype is tested, showing experimental results that align closely with simulations, confirming the effectiveness of the decoupling mechanism in dual windings.**

***Index Terms*—dual-mechanical-port dual-electrical-port machine (DMP-DEPM), hybrid electric vehicles, radial flux (RF), transverse flux (TF).**

I. Introduction

With the development of high-power electric drives such as electric vehicles, magnetic levitation railroads and naval electric drives, as well as high-power wind power generation, electrical continuously variable transmission device-dual mechanical port machine (DMPM), has attracted more and more attention due to its merits such as compactness [1], high power density, high efficiency [2], etc. In general, DMPMs have two mechanical ports and one or more electrical ports, providing favorable conditions for distributing or combining energy from different ports [3]. The DMPM was first proposed to improve the performance of induction machines, but as the flux modulation theory has become more and more popular in the design of DMPMs [4], different types of DMPM have been proposed, such as pseudo-direct-drive machines [5] and bidirectional flux modulation machine [6]. According to the power flow relationships between the two electrical ports and mechanical ports, the DMPMs can be classified into three categories: Series power flow (SPF) type machines, Parallel power flow (PPF) type machines, and Hybrid power flow (HPF) type machines [7]. Among them, the proposed hybrid-flux dual-mechanical-port and dual-electrical-port machine (DMP-DEPM) belongs to the HPF category. Besides, DMPMs are widely used in a wide range of applications such as hybrid electric vehicles [8]-[9], wind power generation [10]-[11], aircraft propulsion [12] and robotic actuators due to their characteristics of flexible energy conversion and distribution, functional diversity and integration, improved system reliability and redundancy, etc. However, due to the special structure of the DMPMs, the disadvantage of coupled electric load and inconvenient multipole/multiphase design exists.

The multipole/multiphase machine is usually accompanied by two sets of winding, and if the two sets of winding cannot be decoupled, the two sets of winding will generate magnetic potentials that interfere with each other. Therefore, it may affect the machine torque ripple increases, efficiency decreases, stability deteriorates and other problems. Although it is possible to decouple two sets of winding through the machine control, it also increases the complexity of the control and makes the machine control less stable.

On the contrary, the transverse flux machine (TFM) has the merit of high torque/power density [13]-[14], decoupled electric load and a magnetic load, ending-free winding [15], and convenient multipole/multiphase design [16]. Numerous studies in the literature have delved into TFMs, encompassing structural innovations, electromagnetic modelling, design optimization, and related aspects [17]-[18]. TFMs can be combined with different types of machines to create new machine types, which can be categorized as flux-switching TFMs (FS-TFMs) [19]-[20], Vernier TFM (V-TFMs) [21],

Manuscript received December 11, 2024; revised May 26, 2025, July 18, 2018; accepted July 7, 2025. *(Corresponding author: Shuangxia Niu.)*
Ziqi Huang, Mingyuan Jiang, Shuangxia Niu, Zekai Lyu, Wenjie Wu, and Longfei Xiao are with the Department of Electrical and Electronic Engineering, The Hong Kong Polytechnic University, Hong Kong SAR, 999077, China.

e-mail: purpleflag.huang@connect.polyu.hk; m.y.jiang@polyu.edu.hk; eesxniu@polyu.edu.hk;zekai.lyu@polyu.edu.hkmail;23072058r@connect.polyu.hk;23125981@connect.polyu.hk).

flux-reversal TFMs (FR-TFMs) [22]-[23]. In general, the TFMs are widely used in large-torque low-speed applications [24]-[25]. However, this type of machine is not suitable for high-speed applications.

A double rotor transverse flux machine (DRTFM), which can cooperate with a conventional three-phase radial flux permanent magnetic synchronous machine (PMSM) to compose a DMP-DEPM, is investigated in this paper. The three-phase radial flux (RF) coils, the stator, and the outer rotor consist of the conventional radial PMSM. The transverse flux (TF) coils, the stator, the outer rotor, and the inner rotor form a DRTFM. During normal operation, the PMSM is equivalent to an electric machine, and the DRTFM is equivalent to a generator, which replaces the architecture that requires two motors in traditional electrical continuously variable transmission (E-CVT) systems.

In Section II, the machine structure and optimization mechanism of the proposed DMP-DEPM are introduced. The construction of a 3-D finite-element analysis (FEA) has been undertaken, with the performance evaluation of the proposed machine being conducted in Section III. This evaluation encompasses factors such as flux linkage, no-load back electromotive force (EMF) and flux density, with the utilization of Ansys Maxwell. The performance of the proposed machine and the existing DRTFM is compared in Section IV. A prototype of the proposed machine is manufactured, and a series of preliminary experiments have been conducted in Section V to verify the machine's functionality.

II. Machine Structure and Optimization Mechanism

A. Machine Structure

Fig. 1 illustrates the three-dimensional exploded view. The DMP-DEPM machine is composed of a single stator and two rotors (an outer rotor and an inner rotor). In order to achieve decoupling capability, the DMP-DEPM in this paper is designed as a three-phase machine, which is composed of three single-phase components. As shown in Fig. 1, a set of three individual single-phase machine components are arranged axially with an electrical degree difference of 120 degrees between them. In the stator part, 20 individual stator axial flux cores are placed axially at the top of the stator in each phase. Three transverse flux coils are arranged independently in the yoke of the three-phase stator.

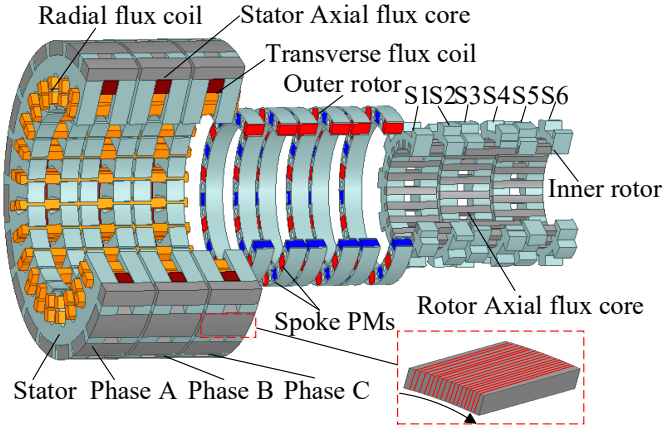

Fig. 1 Exploded view of the proposed DMP-DEPM.

It is worth mentioning that a special stacking method is used for the stator axial flux core and the rotor axial flux core. This method differs from the conventional stator axial stacking method, in which the silicon steel sheets of the stator axial flux core are stacked along the circumference. As shown by the black arrow within the red box in Fig. 1. Rotor axial flux core can be made of carbon steel cast in one piece as the cross-sectional area is too small.

As can be seen from the outer rotor part, the opposite magnetization PMs are arranged in a spoke-type configuration, with all of them magnetized in the tangential direction. The inner rotor part is the most complex component in the proposed machine.

To better illustrate this structure, the inner rotor is divided into six segments, S1, S2, S3, S4, S5, and S6, with an electrical angle difference of 180 degrees between S1 and S2, S3 and S4, S5 and S6. In addition, the difference in electrical angle between S1, S3, and S5 is 120 degrees, which represents a difference of 120 degrees in electrical angle between the three phases A, B, and C.

The configuration of the double-layer radial flux coil winding connection is illustrated in Fig. 2. The proposed machine can be conceptualized as a combination of a traditional PMSM and a TFM. The PMSM form of the RF coils, stator and outer rotor. The three-phase alternating current was injected into the three-phase TF coils. The TF coils, stator, outer rotor, and inner rotor are all components of a TFM.

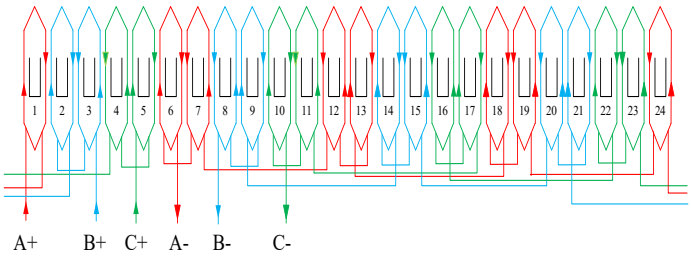

Fig. 2 Configuration of radial flux coil of the proposed DMP-DEMP.

In the realm of power-split-type hybrid electrical devices, the E-CVT system plays a pivotal role. It serves as a sophisticated power management hub, enabling seamless combination and distribution of power among the mechanical input, electrical port, and battery pack. Moreover, it effectively decouples input speed, output speed, and torque, optimizing the overall efficiency of the hybrid powertrain.

For mild hybrid vehicles, which commonly incorporate power split devices as extensively documented in references [26]-[28], both the internal combustion engine (ICE) and the proposed electric machine offer versatile propulsion options. They can operate independently to drive the vehicle or collaborate synergistically to meet varying driving demands. In contrast, conventional CVT systems typically necessitate two distinct machines, one functioning in electric machine mode and the other in generator mode, leading to more complex mechanical architectures.

To overcome these structural limitations, the E-CVT system has been innovatively developed. Featuring a unique design with two mechanical ports and two electrical ports, it

excels at torque and winding decoupling. As depicted in Fig. 3, the inner rotor is mechanically linked to the ICE, serving as the input mechanical port, while the outer rotor is connected to the load, such as vehicle wheels, acting as the output mechanical port. Using its dual winding structure, the proposed prototype can precisely control the speed and torque of the mechanical output ports as well as realize both electric machine mode and generator mode functions, thus improving the dynamic performance and fuel economy of the mild hybrid vehicle.

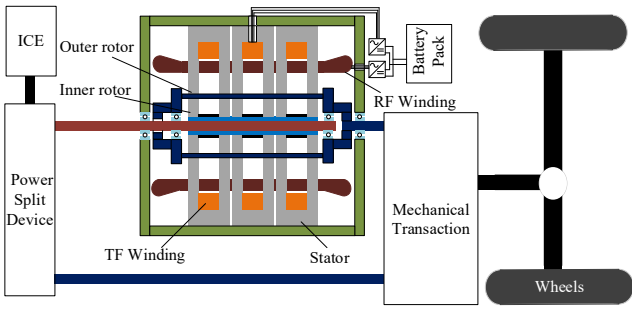

Fig. 3 Configuration of the proposed DMP-DEPM based E-CVT system.

As illustrated in Fig. 4, the petrol from the petrol station is transferred into the petrol tank, thereby powering the ICE. The battery can be recharged by the charging station, or alternatively, it can be recharged during operation by the windings of the proposed machine. The battery supplies power to the DMP-DEPM, which converts electrical energy into mechanical energy via its windings and rotors, driving the wheels through mechanical transmission.

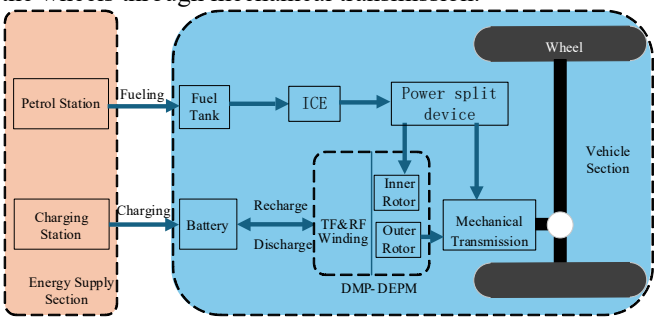

Fig. 4 Energy flow chart.

B. Operation Principle

To grasp the operational principle of the proposed DMP-DEPM, a novel topology, it is helpful to view it as a fusion of a conventional PMSM and a DRTFM. The conventional PMSM comprises three-phase RF coils, the stator, and the outer rotor. Meanwhile, the DRTFM includes TF coils, the stator, the outer rotor, and the inner rotor.

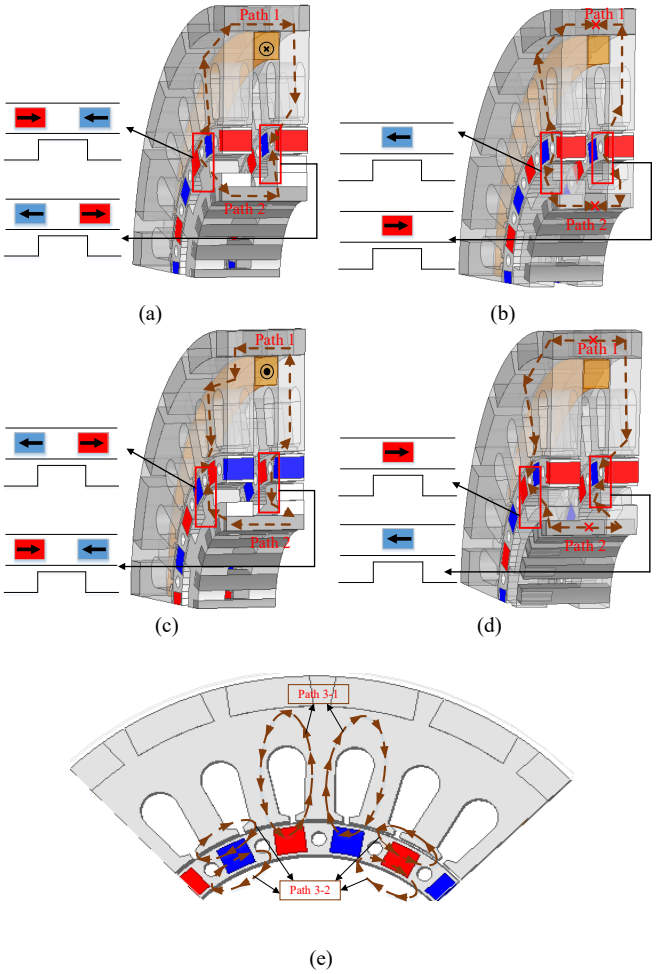

Fig. 5 Flux patterns of DMP-DEPM at different rotor positions. (a) Initial position, θ_{TF}=0 (b) θ_{TF}=90° (c) θ_{TF}=180° (d) θ_{TF}=270° (e) Side view.

In order to present the operation principle of the part of a double rotor transverse flux machine (DRTFM), the working flux varying with the outer rotors and inner rotors under spoke type of PMs array is presented in Fig. 5 Four special states of the electrical angle of the transverse flux coil θ_{TF} are explained by means of a simplified local model. As can be seen in Figs. 5(a) and (c), in these two positions, the teeth of the inner rotors are aligned with the PMs so that an anisotropic magnetic circuit occurs in the axial flux cores of the outer rotors and inner rotors, preventing the formation of a complete electromagnetic circuit. As can be seen in Figs. 5(b) and (d), in these two positions, the teeth of the inner rotors are aligning the central axis of adjacent PMs so that the magnetic circuit goes from the PMs through the axial flux cores of the outer and inner rotor back to the outer rotor of the same phase respectively. In addition, from Fig. 5(e), the PMs have self-leakage into the outer rotor and inner rotor through Path 3-1 and Path 3-2, respectively.

C. Magnetic Circuit

The equivalent magnetic circuit (EMC) model serves as a valuable tool for assessing a novel machine design in its initial design stage. The model is derived from the basic magnetic circuit unit representing the mobile PM excitation considering only one pair of PM poles case. From this EMC model, it can

be found that there are two radial magnetic return paths and one axial magnetic return path for each pole pair PM excitation. Here, we take one pole-pair for EMC analysis, shown in Fig. 6, where F_{PM} is the PM magnetomotive force (MMF). φ_{TF_1} and φ_{TF_2} are the flux linkages passing through two radial magnetic return paths. R_{go} and R_{gi} are the air gap reluctance in the common return path for the outer airgap and inner airgap respectively. $R_{\sigma 1}$, $R_{\sigma 2}$ are the flux leakage of axial magnetic return path 1,2 respectively. $R_{\sigma 3}$ is the flux leakage of the radial magnetic return path.

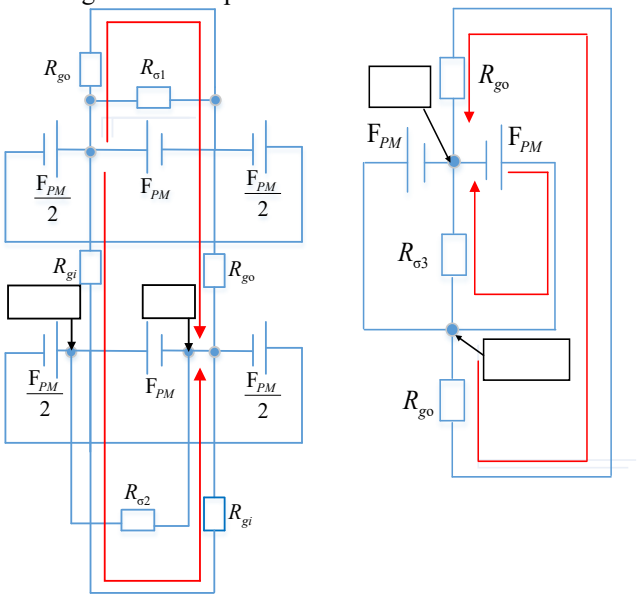

(a) (b)

Fig. 6 Equivalent Magnetic Circuit. (a) Equivalent transverse flux magnetic circuit. (b) Equivalent radial flux magnetic circuit.

As can be seen from Fig. 6(a), when the magnetic saturation is ignored, the flux for the transverse magnetic field under no-load condition can be expressed as follows:

$$\begin{cases} \varphi_{TF_1} = \dfrac{F_{PM}}{\dfrac{2R_{go}R_{\sigma 1}}{2R_{go}+R_{\sigma 1}}} sin(\omega_{TF}t) \\ \varphi_{TF_2} = \dfrac{F_{PM}}{\dfrac{R_{gi}R_{\sigma 2}}{2R_{gi}+R_{\sigma 2}}} sin(\omega_{TF}t) \end{cases} \quad (1)$$

As can be seen from Fig. 6(b), the flux for the radial flux magnetic field under no-load condition can be expressed as follows:

$$\begin{cases} \varphi_{RF_1} = \dfrac{F_{PM}}{2R_{go}} sin(\omega_{RF}t) \\ \varphi_{RF_2} = \dfrac{F_{PM}}{R_{\sigma 3}} sin(\omega_{RF}t) \end{cases} \quad (2)$$

where ω_{RF} and ω_{TF} are the electrical angular velocity for RF winding and TF winding respectively.

$$\omega_{TF} = 2\pi f_{TF}, \qquad f_{TF} = N_{p\_PM}\frac{|n_i - n_o|}{60} \quad (3)$$

$$\omega_{RF} = 2\pi f_{RF}, \quad f_{RF} = \frac{N_{p\_PM}n_o}{60} \quad (4)$$

where N_{p_PM} is the number of pole pair PMs circuit in a single phase, n_i and n_o represent the rotating speed for the inner rotor and outer rotor respectively.

φ_{TF_1} and φ_{RF_1} are working flux linkage, the single-phase flux linkage for RF winding and TF winding can be expressed as follows:

$$\varphi_{a\_TF} = N_{p\_PM}N_{TF}\frac{F_{PM}}{\dfrac{2R_{go}R_{\sigma 1}}{2R_{go}+R_{\sigma 1}}} sin(\omega_{TF}t) \quad (5)$$

$$\varphi_{a\_RF} = N_{p\_PM}N_{RF}\frac{F_{PM}}{2R_{go}} sin(\omega_{RF}t) \quad (6)$$

where N_{TF} and N_{RF} are the number turns of TF winding coils and RF winding coils respectively.

Using Faraday's Law, the corresponding No-load single-phase back EMF for RF winding and transverse flux winding can be further obtained as follows:

$$E_{phase\_TF} = -N_{t\_TF}\frac{d\varphi_{a\_TF}}{dt} \quad (7)$$

$$E_{phase\_RF} = -N_{t\_RF}\frac{d\varphi_{a\_RF}}{dt} \quad (8)$$

$$P_{total} = 3E_{phase\_TF}I_{TF} + 3E_{phase\_RF}I_{RF} \quad (9)$$

where N_{t_TF} is the number of turns of TF winding, N_{t_RF} is the number of turns of RF winding. P_{total} is the total power of the proposed machine. E_{phase_TF} and E_{phase_RF} are the Phase voltage of the TF winding and RF winding respectively. I_{TF} and I_{RF} are the the RMS value of the TF winding and RF winding respectively.

$$T_{e_{total}} = \frac{3E_{phase\_RF}I_{RF}}{\Omega_o} + \frac{3E_{phase\_TF}I_{TF}}{|\Omega_i - \Omega_o|} \quad (10)$$

where $T_{e_{total}}$ is the the total torque produced by the proposed machine. Ω_i and Ω_o represent the mechanical speed of the inner rotor and outer rotor respectively.

The newly developed EMC model allows for the rapid prediction of the back EMF of this innovative topology. Additionally, the average torque can be accurately estimated, as it is directly related to the product of the back EMF and current excitation. Consequently, this EMC model can be utilized during the preliminary selection of design parameters, as the 3-D finite-element calculation is a time-consuming process. The novel topology parameters and optimization results are described in detail in Section II.D.

D. Optimization Process

In contrast to conventional machinery, the flux of the stator and inner rotor in the proposed DMP-DEPM is distributed in 3-D directions, thereby resonating the utilization of the machine's axial flux. Consequently, a 3-D finite-element model of the DMP-DEPM has been constructed for the purpose of investigating the machine's performance. At this stage, it is necessary to determine some of the main invariant design parameters, such as the stator outer diameter, the machine axial length, and the air gap, in order to provide guidance for the design. The main optimization objectives are to maximize the

torque of the inner rotor and outer rotor and minimize the inner rotor and outer rotor torque ripple, with the aim of achieving a compact design. Some general dimension parameters of the proposed topology are given in Fig. 7, and their design values are listed in Table I. The stator outer diameter is fixed at 210 mm, and the length of the whole machine is fixed at 109 mm.

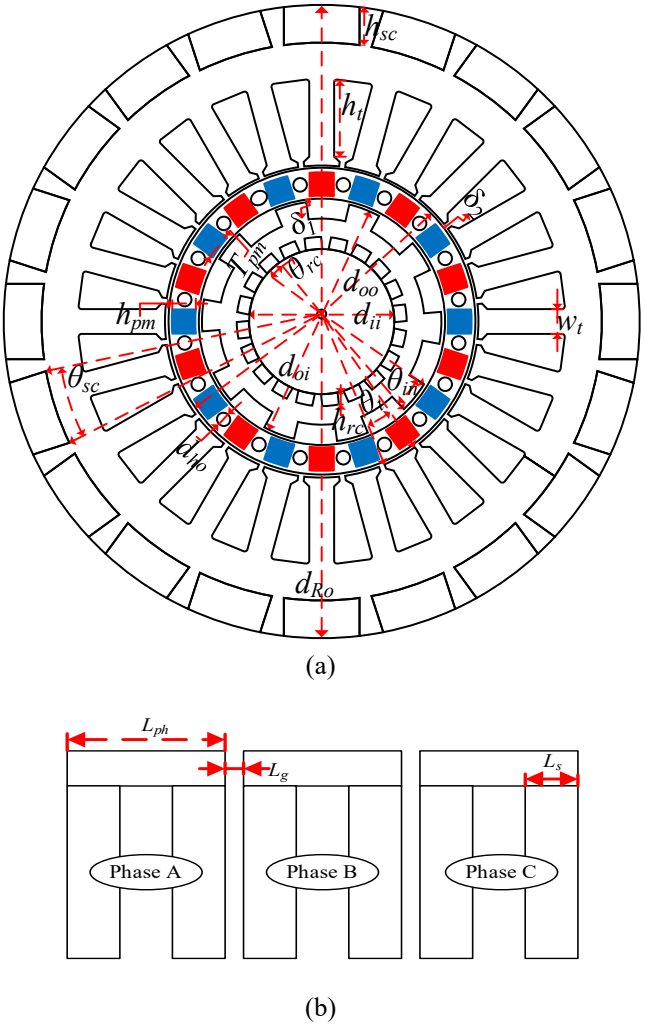

Fig. 7 Dimensions. (a) Radial view. (b) Stator Circumferential view.

The optimization flowchart is presented in Fig. 8. The whole process is based on the condition of double rotor counter rotation and the current density of all windings at 6A/mm^2. In order to achieve suitable parameters for the proposed design, it is necessary to optimize the geometric parameters of the DMP-DEMP model. The objectives of all optimization processes are based on the maximization of the outer rotor output torque density, denoted T_{den}, and the minimization of the maximum torque ripple ratio, denoted T_{rip}. The definitions of $T_{den}$and T_{rip} are as follows:

$$T_{den} = \frac{T_{do\_avg}}{V} \tag{11}$$

$$T_{rip} = \frac{\max(T_{ri}, T_{ro})}{T_{do\_avg}} \tag{12}$$

where T_{do_avg} is the average torque of the outer rotor, V is the electromagnetic part volume of the machine, T_{ri} and T_{ro} are the peak-to-peak torque ripple of inner rotor and outer rotor, respectively.

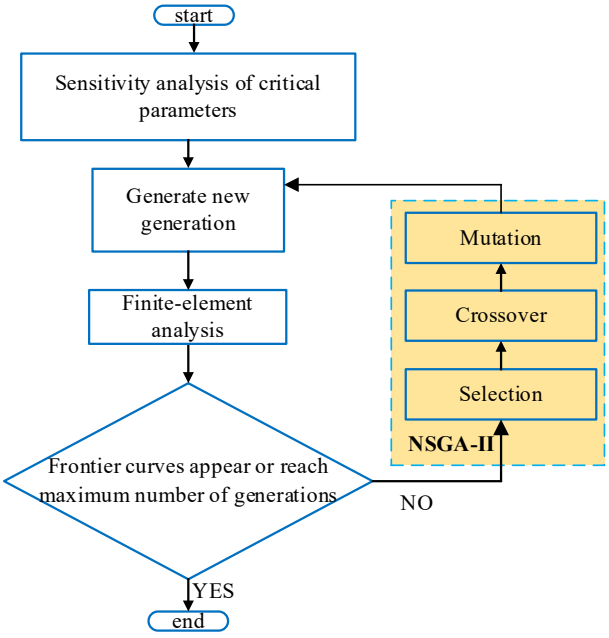

Fig. 8 Optimization flowchart.

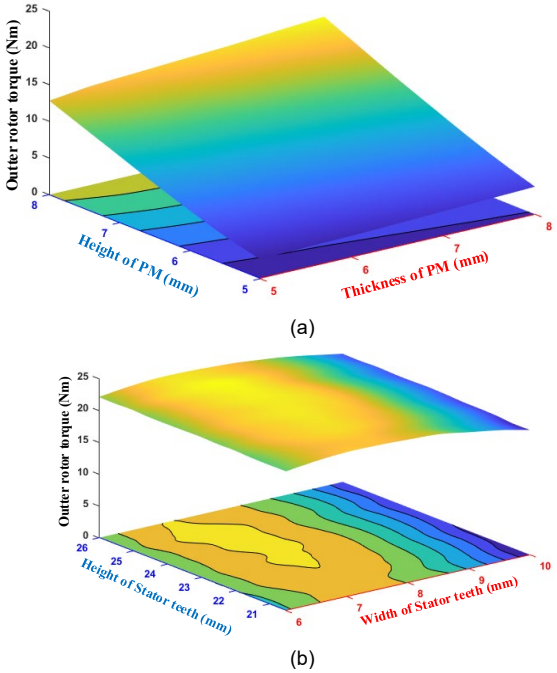

Fig. 9 Influence of design parameters. (a) Influence of design parameters related to PMs. (b) Influence of design parameters related to stator teeth.

According to the optimization flowchart, a hierarchical optimization approach is used to optimize the important and the secondary important parameters separately. Firstly, the FEA is employed to conduct a sensitivity analysis of critical parameters. This process enables the determination of specific values for important parameters.

While increasing the size of PMs is beneficial for improving MMF and increasing the outer rotor torque, as shown in Fig. 9(a), it is accompanied by increased manufacturing difficulty and cost, as well as increased

equivalent reluctance and leakage. Besides, the dimensions of the PMs were selected to be 8mm in height and thickness, with a connection hole of 4.5mm diameter reserved directly for the adjacent outer rotor PMs, in order to meet the machine's assembly requirements.

TABLE I
OPTIMIZED VALUES AND RANGE OF VARIATION OF PROPOSED MACHINE PARAMETERS

Symbol	Quantity	Range of optimization	Optimal design
h_{sc}	Height of axial stator flux core	12.5mm	
h_t	Height of stator teeth	20-26mm	24.7mm
θ_t	Central angle of stator teeth	7-10deg	8.8deg
d_{Ro}	Diameter of stator	210mm	
θ_{sc}	Central angle of stator axial flux core	12-14deg	13.4deg
δ_1	Outer airgap	1mm	
δ_2	Inner airgap	1mm	
d_{ii}	Inner diameter of inner rotor	48.1mm	
d_{ho}	Diameter of hole of outer rotor	4.5mm	
w_t	Width of stator teeth	6-10mm	8.2mm
d_{oi}	Outer diameter of inner rotor	79.5mm	
h_{PM}	Height of PMs	5-8mm	8mm
T_{PM}	Thickness of PMs	5-8mm	8mm
h_{rc}	Height of the rotor axial flux core	4mm	
θ_{rc}	Central angle of rotor axial flux core	4-6deg	5.3deg
θ_{in}	Central angle of inner rotor teeth	6.5-9.5deg	9deg
d_{oo}	Outer diameter of outer rotor	101.5mm	
L_{ph}	Axial length for single phase	35mm	
L_g	Distance between two adjacent phases	2mm	
L_s	Axial length for single phase one side stator	12.5mm	

In addition, the magnetic circuits of the hybrid excitation all pass through the stator teeth, and the choice of stator teeth dimensions also has an essential influence on the electromagnetic performance of the machine. On the one hand, an increase in stator teeth height will inevitably lead to a reduction in the radius of the outer and inner rotors, which will only affect the torque of the outer and inner rotors. On the other hand, if the rotor width is too small, magnetic saturation will easily occur, reducing the output torque. As shown in Fig. 9(b), the stator teeth width is chosen to be around 8 mm to obtain a relatively large outer rotor torque.

After sensitivity analysis, the FEA is utilized with the non-dominant sorting genetic algorithm II (NSGAII) to ascertain the secondary significant parameter value. Moreover, the parameters of the prototype and the range of parameters being optimized are exhibited in Table I.

III. PERFORMANCE EVALUATION

A. No-Load Performance Evaluation

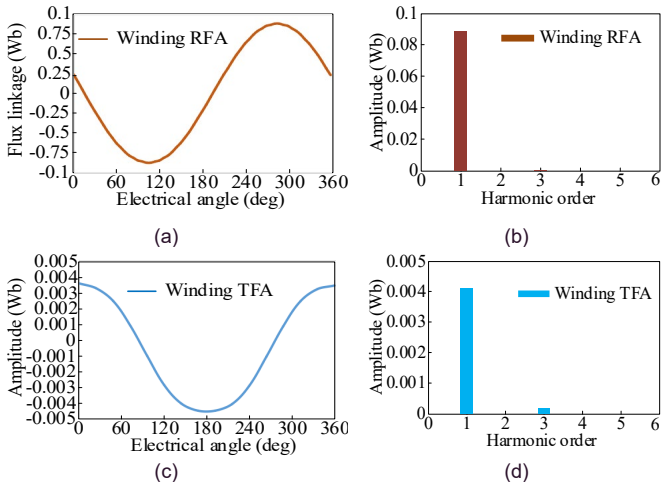

Fig. 10 No-load Phase A flux linkage for speed of 200rpm. (a) Flux linkage of Phase A RF winding (b) Fast transfer analysis of flux linkage of Phase A RF winding (c) Flux linkage of Phase A TF winding (d) Fast transfer analysis of flux linkage of Phase A TF winding.

After optimization, the phase A flux linkage of the RF winding and TF winding for the proposed machine is shown in Fig. 10(a) and Fig. 10(c), respectively. Combined with the Fourier analysis of Fig. 10(b) and Fig. 10(d) for phase A flux linkage of the RF winding and TF winding, respectively, it can be seen that there is the dominant harmonic component in the flux linkage is only the 1st order one, which accordingly makes its wave-good sinusoidal degree. The Total Harmonic Distortion (THD) of the RF winding is about 0.56%, and the THD of the TF winding is about 3.51%. Therefore, the flux linkages of both radial and transverse windings exhibit good sinusoidal characteristics.

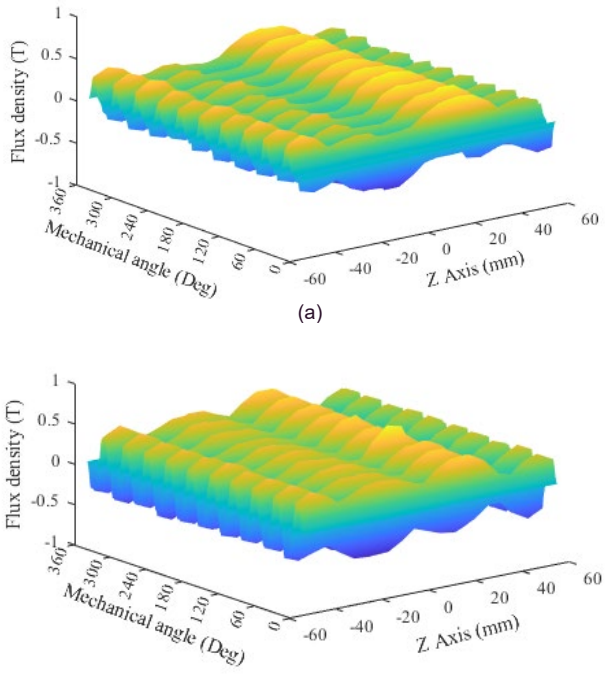

Fig. 11 Airgap flux density. (a) Inner airgap. (b) Outer airgap.

The air gap flux density analysis of the inner rotor and outer rotor is illustrated in Figs. 11(a) and (b), respectively. As demonstrated in Fig. 1, due to the presence of intervals between S1 and S3, and between S4 and S5, there is only flux leakage at these intervals. The air gap flux density of these two segments is predominantly 0, which is also the reason for the trough of the Z axis.

B. On-Load Performance Evaluation

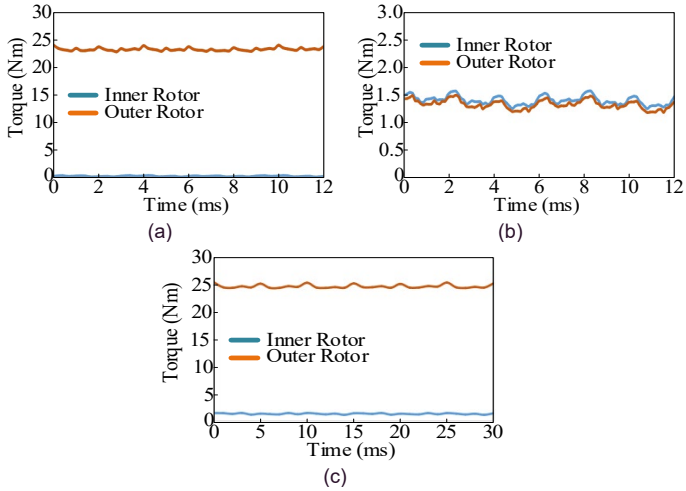

Fig. 12 Torque of inner rotor and outer rotor. (a) RF winding current density is 6A/mm^2 and TF winding is 0. (b) RF winding is 0 and TF winding is 6A/mm^2. (c) Both RF winding current and TF winding current density are 6A/mm^2.

As illustrated in Fig. 12(a), only the RF winding injected with current is equivalent to a conventional PMSM where only the outer rotor has torque. Besides, only the TF winding injected with current is equivalent to a DRTFM where the outer and inner rotor both have almost the same torque, as shown in Fig. 12(b), proving that both mechanical ports get basically the same energy distribution. When the RF and TF winding are injected 6A/mm^2 current, the outer rotor and inner rotor output average torque are 24.3 Nm and 1.2 Nm, respectively, as shown in Fig. 12(c). In addition, the inner rotor torque ripples under 30%, and the outer rotor torque ripples under 5%.

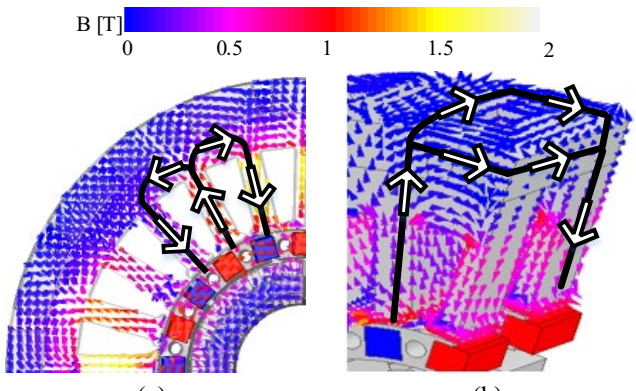

Fig. 13 Flux-density vector distribution in DMP-DEPM. (a) side view. (b) trimetric view.

In the 3D simulation of Figs. 13(a) and(b), the vector of the flux density distribution shows that the magnetic circuit of the core is not saturated when both sets of winding are inputted with a rated current of 6A/mm^2. It also reflects the effective magnetic circuit of radial and transverse windings. As depicted in Fig. 13(a), the effective magnetic circuit of the radial flux needs to pass through the air gaps twice. In an effective transverse magnetic circuit, as illustrated in Fig. 13(b), the magnetic flux traverses one stator tooth, propagates axially through the stator core, and returns via the adjacent stator tooth on the opposite side.

C. Decoupling Analysis

In order to verify the decoupling performance of the proposed machine, two sets of winding are injected with current in turn to verify their decoupling capability. In case I, the RF winding injects a current with a current density of 6A/mm^2, the outer rotor at 500 rpm and the inner rotor speed at -500 rpm; in case II, the TF winding injects a current with a current density of 6A/mm^2, the inner rotor speed is -500 rpm, and the outer rotor speed is 0 rpm.

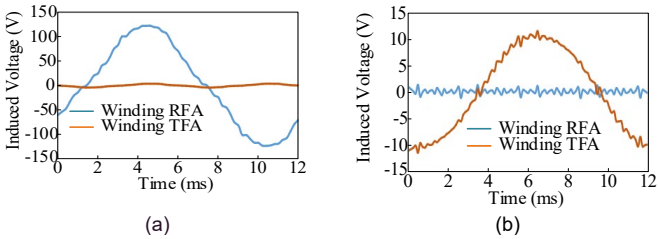

Fig. 14 Decoupled analysis by FEA. (a) Case I. (b) Case II.

As shown in Fig. 14(a), the induced voltage of the TF winding of case I is very small due to the fact that when the outer rotor rotates, the TF winding also generates a tiny back EMF. For case II, only the inner rotor rotates, and the TF winding is injected current. The induced voltage of the RF winding is almost zero, as shown in Fig. 14(b). Two case simulation results corroborate that the proposed machine has a distinguished decoupling performance.

IV. Conventional Structure And Performance Comparison

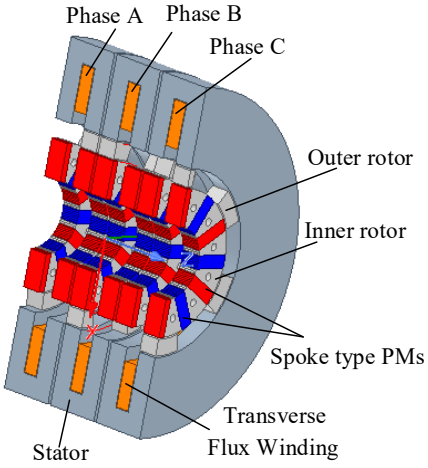

Fig. 15 The existing DRTFM is applied to the hybrid vehicle [29].

TABLE II
MAIN SPECIFICATION OF CONVENTIONAL DRTFM AND PROPOSED MACHINE

Quantity	Topology from [29]	Proposed machine
Diameter of stator	210mm	
Outer airgap	1mm	
Inner airgap	1mm	
Outer diameter of inner rotor	79.5mm	
Height of PMs	19mm	8mm
Thickness of PMs	5mm	8mm
PMs pole pairs	6	10
Outer diameter of outer rotor	101.5mm	
Axial length for single phase	35mm	
Distance between two adjacent phases	2mm	
Axial length for single phase one side stator	12.5mm	
Current density	6A/mm^2	
Outer rotor speed	1000rpm	
Inner rotor speed	-1000rpm	

A conventional DRTFM design in [29] is shown in Fig. 15, which only has the TF windings and is equivalent to a single electrical port, dual mechanical port machine. The proposed design in this paper is a DMP-DEPM.

The proposed machine structure innovatively integrates a PMSM with a DRTFM configuration, distinguishing it from conventional TFM. The proposed machine is equipped with two electrical ports, which means that it can function as a generator and an electric motor simultaneously. During normal operation, the PMSM, composed of RF winding, outer rotor, and stator, is equivalent to an electric motor. The TFM, composed of TF winding and inner rotor, outer rotor, and stator, is equivalent to a generator.

In contrast, the conventional DRTFM single electric port designs require frequent switching between electric motor and generator modes.

In addition, the torque density and efficiency of the proposed topology are improved over the conventional TFM in electric machine mode.

For a fair comparison, the main parameters of the existing TFM are compared with those of the proposed prototype, as shown in Table II.

In the electric machine mode, the PM output torque per volume of the proposed machine is improved from 101.67Nm/L to 256.6Nm/L, and the efficiency is improved from 55.13% to 86.76% compared to the existing DRTFM in the [29].

V. EXPERIMENTAL VERIFICATION

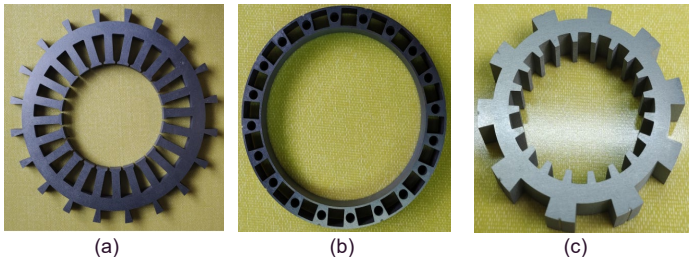

(a) (b) (c)

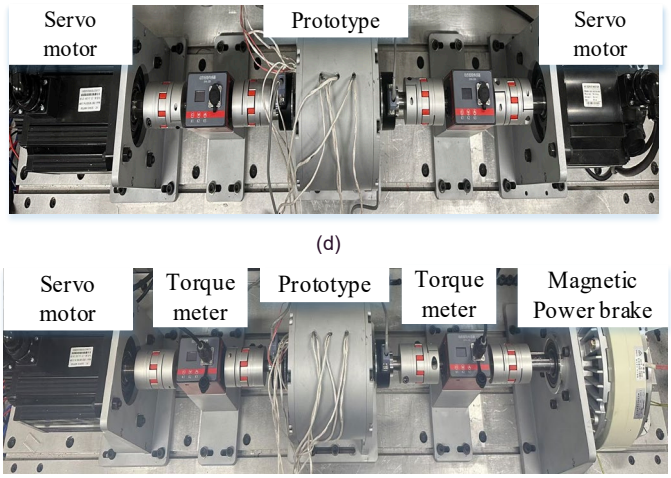

(d)

(e)

Fig. 16 Prototype main parts and the test rigs. (a) Stator core. (b) Outer rotor core. (c) Inner rotor core. (d) Test bench-I. (e) Test bench-II.

A prototype of the proposed machine has been constructed, and experimental procedures have been undertaken in order to validate the theoretical analysis and FEA results. In order to circumvent magnet demagnetization under conditions of extreme operational circumstances, the PM material employed in the prototype is N40UH. Furthermore, the stator, outer rotor core and inner rotor core materials have been selected as DW310-35, as shown in Figs. 16(a), (b) and (c), respectively. In order to increase the stability of the mechanical structure, the outer rotor core structure is reserved with holes for connecting rods, which makes it easy to connect each segment of the outer rotor together.

The two sets of test benches are shown in Figs. 16(d), (e). Fig. 16(d) contains two servo machines, which can satisfy the case of no-load experiment. Fig. 16(e) contains one servo machine and one magnetic power brake, which can not only satisfy the load experiment's case but also simulate the proposed scheme. The inner rotor is connected to the servo machine, which acts as a prime mover, and the magnetic power brake is connected to the outer rotor, which can act as a load.

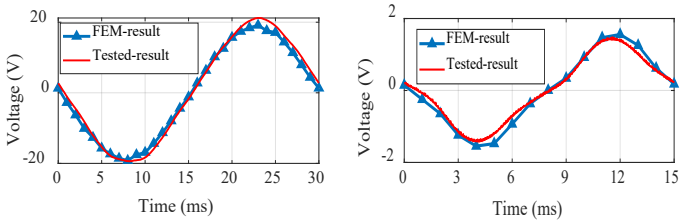

(a) (b)

Fig.17. Comparison of the measured back EMF and the result of FEA. (a) phase A back EMF of RF winding. (b) phase A back EMF of TF winding.

The no-load phase back EMF of the proposed machine is measured at a constant speed of the inner rotor at 200 rpm and the outer rotor at -200 rpm. The comparison of the no-load back EMF is shown in Figs. 17(a) and (b), and the two sets winding actual waveform is greatly consistent with that of the FEA.

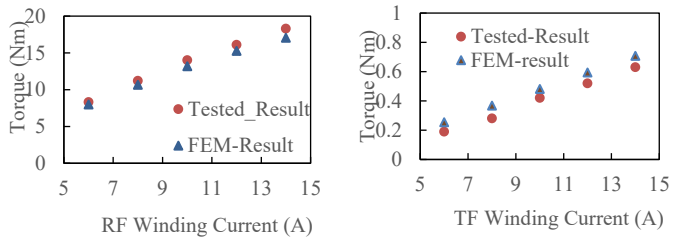

Fig. 18 Measured torque-current waveforms. (a) Outer rotor torque. (b) Inner rotor torque.

The output torque versus current curves for the outer and inner rotor currents are shown in Figs. 18(a), (b). The obtained torque is basically in accordance with the results of the 3D simulation. Nevertheless, a number of experimental errors cannot be exactly model building or forecast in a simulation. That may be due to the cutting process of the silicon steel sheet, the friction torque on the shaft, the effect of imperfect sinusoidal current with some distortion, etc.

As shown in Fig. 19(a), the inner rotor is dragged by the servomotor to rotate at a speed of 200 rpm, the RF winding current equals zero, and the TF winding generates a back EMF. Subsequently, currents of 1A, 2A and 3A are injected into the RF winding, respectively, as demonstrated in Figs. 19(b), (c) and (d), causing the outer rotor to rotate at -200 rpm. Because of the modulation effect of the outer rotor, the back EMF of the TF winding doubles, but the current increase of the RF winding has basically no effect on the amplitude of the back EMF of the TF winding, which proves the decoupling performance of the two sets of winding.

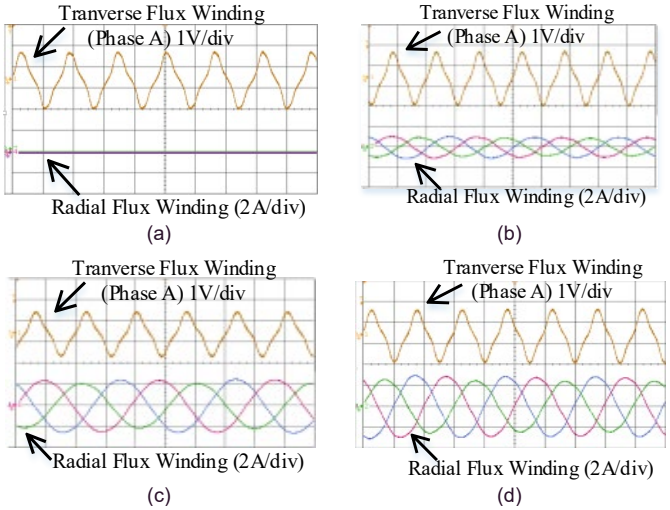

Fig. 19 Decoupling verification experiments. (a) RF Winding input current=0A. (b) RF Winding input current=1A. (c) RF Winding input current=2A. (d) RF Winding input current=3A.

In variable speed experiment A, the inner rotor—driven by the prime mover—rotates at 600 rpm, with an external load of 5.8 Nm applied. The RF winding is injected with current to control the outer rotor to rotate in the opposite direction, and the speed rises from 500 rpm to 600 rpm, as shown in Fig. 20(a). As illustrated in Fig. 20(b), a significant fluctuation in the torque ripple of the outer rotor torque is observed in response to variations in the speed. As demonstrated in Fig. 20(c), the amplitude of the RF winding is subject to alteration. The current amplitude exhibits an increase in response to significant variations in outer rotor torque. Subsequently, the fluctuation recovers rapidly, indicating a dynamic response of the system to changes in operation.

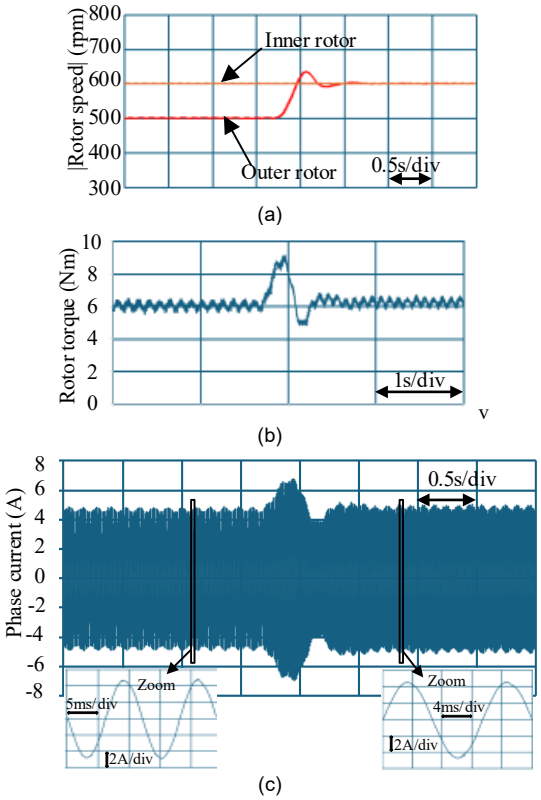

Fig. 20 Speed variation experiment experiments under 5.8 Nm load. (a) Speed of inner rotor and outer rotor. (b) Outer rotor torque. (c) RF Winding (Phase A) input current.

In experiment B, the inner rotor speed was maintained at 600 rpm while the external load was increased to 10.4 Nm. As demonstrated in Fig. 21(a), an increase in the outer rotor speed from 600 rpm to 700 rpm was observed. As demonstrated in Fig. 21(b), during the process of speed rise, the outer rotor torque ripple greatly increases and rapidly recovers to within 10%. As demonstrated in Fig. 21(c), the amplitude of the RF winding undergoes a sharp increase during the process of torque oscillation. Thereafter, the amplitude returns to its standard level once the torque ripple reverts to its stable state.

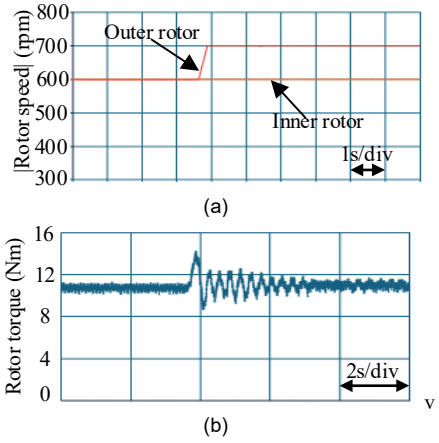

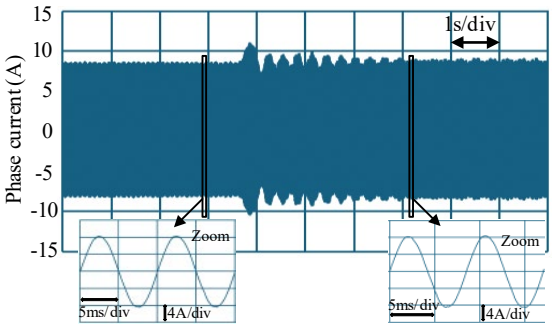

(c)

Fig. 21 Speed variation experiment experiments under 10.4 Nm load. (a) Speed of inner rotor and outer rotor. (b) Outer rotor torque. (c) RF Winding (Phase A) input current.

VI. CONCLUSIONS

A novel hybrid flux dual mechanical port machine structure using a novel radial magnetic path and an axial magnetic path has been investigated to solve the decoupling problem for two sets of winding of the double rotor machine. This dual-electrical-port configuration effectively overcomes the shortages of single-electrical-port transverse flux machines in hybrid electric vehicles, enabling the machine to function concurrently, working as a motor and a generator. In motor mode, the proposed machine demonstrates superior torque density and efficiency compared to DRTFM. Given its specific design features, this machine is particularly well-suited for specialized applications, such as mild hybrid electric vehicles.

REFERENCES

[1] S. Niu, Y. Liu, S. L. Ho and W. N. Fu, "Development of a Novel Brushless Power Split Transmission System for Wind Power Generation Application," *IEEE Trans. Magn.*, vol. 50, no. 11, pp. 1-4, Nov. 2014.

[2] H. Chen, A. M. EL-Refaie, Y. Zuo, S. Cai, L. Cao and C. H. T. Lee, "Comparative Study and Design Optimization of a Dual-Mechanical-Port Electric Machine for Hybrid Electric Vehicle Applications," *IEEE Trans. Veh. Technol.*, vol. 71, no. 8, pp. 8341-8353, Aug. 2022.

[3] S. Niu, S. L. Ho, and W. N. Fu, "A novel double-stator double rotor brushless electrical continuously variable transmission system," *IEEE Trans. Magn.*, vol. 49, no. 7, pp. 3909–3912, Jul. 2013.

[4] Y. Mao, S. Niu, and Y. Yang, "A new parameter identification method of a dual-rotor flux-modulation machine based on an adaptive differential evolution algorithm," *IET Renew. Power Gener.*, vol. 15, no. 9, pp. 1888–1897, Jul. 2021.

[5] Q. Gan, Y. Fang and P. -D. Pfister, "A Novel Concentrated-Winding Vernier Pseudo-Direct-Drive Permanent-Magnet Machine," *IEEE Transactions on* Magnetics, vol. 58, no. 2, pp. 1-5, Feb. 2022.

[6] Y. Wang, S. Niu, and W. Fu, "Sensitivity Analysis and Optimal Design of a Dual Mechanical Port Bidirectional Flux-Modulated Machine," *IEEE Transactions on Industrial Electronics*, vol. 65, no. 1, pp. 211-220, 2018.

[7] M. Jiang and S. Niu, "Overview of Dual Mechanical Port Machines in Transportation Electrification," *IEEE Transactions on Transportation Electrification*, vol. 10, no. 3, pp. 4959–4977, Oct. 2023.

[8] P. Zheng, Q. B. Zhao, J. G. Bai, B. Yu, Z. Song, J. Shang, "Analysis and design of a transverse-flux dual rotor machine for power-split hybrid electric vehicle applications," *ENERGIES*, vol. 6, no. 12, pp. 6548–6568, Dec. 2013.

[9] M. Jiang and S. Niu, "A High-Order Harmonic Compound Rotor Based Brushless Dual-Electrical-Port Dual-Mechanical-Port Machine," in *IEEE Transactions on Industrial Electronics*, vol. 71, no. 6, pp. 5463-5473, June 2024.

[10] H. Chen, A. M. EL-Refaie, Y. Zuo, S. Cai, S. Xie and C. H. T. Lee, "Evaluation of a Contra-Rotating Flux- Modulated Machine Featured With Dual Flux-Modulation for Wind Power Generation," in *IEEE Transactions on Industrial Electronics*, vol. 69, no. 9, pp. 8770-8781, Sept. 2022.

[11] M. Jiang, S. Niu and C. Chuen Chan, "A High-Order-Harmonic Compound-Rotor Based Brushless Doubly-Fed Machine for Variable Speed Constant Frequency Wind Power Generation," in *IEEE Journal of Emerging and Selected Topics in Power Electronics*, vol. 13, no. 2, pp. 1492-1502, April 2025.

[12] H. Zhao, C. Liu, Z. Song, and W. Wang, "Analytical Modeling of a Double-Rotor Multiwinding Machine for Hybrid Aircraft Propulsion," *IEEE Transactions on Transportation Electrification*, vol. 6, no. 4, pp. 1537–1550, Dec. 2020.

[13] X. Yang, B. Kou, J. Luo and H. Zhang, "A Novel Dual-Consequent-Pole Transverse Flux Machine and Its Analytical Modeling," *IEEE Trans. Ind. Electron*., vol. 68, no. 5, pp. 4141-4152, May 2021.

[14] B. Kaiser and N. Parspour, "Transverse Flux Machine—A Review," *IEEE Access*, vol. 10, pp. 18395-18419, 202.

[15] Ballestín-Bernad, V., Artal-Sevil, J. S., & Domínguez-Navarro, J. A. (2021). A Review of Transverse Flux Machines Topologies and Design. *Energies*, *14*(21), 7173.

[16] J. Wang and N. J. Baker, "A linear laminated cylindrical transverse flux machine for use with a free piston engine," *IEEE Trans. Energy Convers.,*vol. 33, no. 4, pp. 1988–1997, Dec. 2018.

[17] A. Ahmed and I. Husain, "Power factor improvement of a transverse flux machine with high torque density," *IEEE Trans. Ind. Appl*., vol. 54, no. 5,pp. 4297–4305, Sep./Oct. 2018.

[18] T. Husain, I. Hasan, Y. Sozer, I. Husain, and E. Muljadi, "Cogging torque minimization in transverse flux machines," *IEEE Trans. Ind Appl*., vol. 55,no. 1, pp. 385–397, Jan./Feb. 2018.

[19] M. Zhao et al., "Development and analysis of novel flux-switching transverse-flux permanent magnet linear machine," *IEEE Trans. Ind. Electron*.,vol. 66, no. 6, pp. 4923–4933, Jun. 2019.

[20] Z. Zhang, X. Tang, C. Zhang and M. Li, "Comparative Study on Modular Longitudinal and Transverse Flux-Switching Permanent Magnet Linear Motor," in *IEEE Transactions on Energy Conversion*, vol. 35, no. 1, pp. 33-42, March 2020.

[21] R. Li, R. Qu, D. Li, Y. Gao and C. Shi, "A Novel Modular Transverse Flux Linear Permanent Magnet Vernier Machine with Halbach Arrays and Consequent Poles," *2019 IEEE Energy Conversion Congress and Exposition (ECCE)*, Baltimore, MD, USA, 2019, pp. 3033-3037.

[22] S. Zhu, T. Cox and C. Gerada, "Comparative study of novel tubular flux-reversal transverse flux permanent magnet linear machine," *2017 IEEE Energy Conversion Congress and Exposition (ECCE)*, Cincinnati, OH, USA, 2017, pp. 4282-4287.

[23] B. Kou, X. Yang, J. Luo, and Y. Zhou, "Modeling and analysis of a transverse-flux flux-reversal machine," *IEEE Trans. Energy Convers*.,vol. 31, no. 3, pp. 1121–1131, Sep. 2016.

[24] Y. -S. Hsu and M. -C. Tsai, "Development of a Novel Transverse Flux Wheel Motor," in *IEEE Transactions on Magnetics*, vol. 47, no. 10, pp. 3677-3680, Oct. 2011.

[25] P. Zheng et al., "Analysis and design of a transverse flux dual rotor machine for power-split hybrid electric vehicle applications," *Energies*, vol. 6,no. 12, pp. 6548–6568, 2013.

[26] J. M. Miller, "Hybrid electric vehicle propulsion system architectures of the e-CVT type," *IEEE Transactions on Power Electronics*, vol. 21, no. 3, pp. 756–767, May 2006.

[27] X. Han et al., "Flexible Energy Conversion Control Strategy for Brushless Dual-Mechanical-Port Dual-Electrical-Port Machine in Hybrid Vehicles," *IEEE Transactions on Power Electronics*, vol. 34, no. 4, pp. 3910–3920, Apr. 2019.

[28] X. Ren, D. Li, R. Qu, W. Kong, X. Han, and T. Pei, "Analysis of Spoke-Type Brushless Dual-Electrical-Port Dual-Mechanical-Port Machine With Decoupled Windings," *IEEE Transactions on Industrial Electronics*, vol. 66, no. 8, pp. 6128–6140, Sep. 2018.

[29] M. Wang, P. Zheng, C. Tong, Q. Zhao and G. Qiao, "Research on a Transverse-Flux Brushless Double-Rotor Machine for Hybrid Electric Vehicles," in *IEEE Transactions on Industrial Electronics*, vol. 66, no. 2, pp. 1032-1043, Feb. 2019.

ZIQI HUANG received his B.Eng. degree in electrical engineering and automation from Southeast University Chengxian College, Nanjing, China, in 2019, and the M.Sc. degree in electrical engineering from The Hong Kong Polytechnic University, Hong Kong, China, in 2021.

He is currently pursuing the PhD degree at the Department of Electrical and Electronic Engineering at Hong Kong Polytechnic University. His main research interests include the design and optimization of novel electric machines.

Mingyuan Jiang received the B.Eng. degree in electrical engineering and automation from Shanghai Maritime University, Shanghai, China, in 2020. Subsequently, he obtained the M.Sc. and Ph.D. degrees in electrical engineering from The Hong Kong Polytechnic University, Hong Kong, China, in 2021 and 2024, respectively.

He is currently a Research Assistant Professor in the Department of Electrical and Electronic Engineering, The Hong Kong Polytechnic University. His primary research focuses on the design, optimization, and control of electric machines, electric vehicles, and power generation.

Shuangxia Niu (Senior Member, IEEE) received the B.Sc. and M.Sc. degrees from Tianjin University, Tianjin, China, in 2002 and 2005, and the Ph.D. degree from the University of Hong Kong, Hong Kong, SAR, China, in 2009, all in electrical engineering.

She is currently a professor with the Department of Electrical and Electronic Engineering, The Hong Kong Polytechnic University. She authored or coauthored more than 200 papers in leading journals. Prof. Niu is currently an Associate Editor for the IEEE Journal of Emerging and Selected Topics in Power Electronics.

Zekai Lyu received the B.Eng. degree from Southwest Jiaotong University, Chengdu, China, in 2018, the M.Sc. degree from Harbin Institute of Technology, Harbin, China, in 2020, and the Ph.D. degree from Zhejiang University, Hangzhou, China, in 2024, all in electrical engineering.

He is currently a Postdoctoral Fellow with the Department of Electrical and Electronic Engineering, The Hong Kong Polytechnic University, Hong Kong SAR, China. His research interests include wide-bandgap device applications, electrical machines, and machine drives.

Wenjie Wu received the B.Sc. degree from Yancheng Institute of Technology, Yancheng, China, in 2019, and the M.Sc. degree from the School of Electrical Information Engineering, Jiangsu University, Zhenjiang, China, in 2023.
He is currently working toward the Ph.D. degree in electrical engineering with The Hong Kong Polytechnic University, Hong Kong.

His current research interests include permanent-magnet machine design and optimization.

Longfei Xiao received his B.Eng. degree from Shanghai DianJi University in 2016, the M.Eng degree from University of Shanghai for Science and Technology in 2020. From 2020-2023, he worked as a machine designer in two technology companies: Fortior Technology (Shenzhen) Co., Ltd and Shanghai Mingzhi Electric Co., Ltd.

He is currently a Ph.D. student with the Department of Electrical and Electronic Engineering, The Hong Kong Polytechnic University, Hong Kong. His main research interests include the EM analysis and design of induction machines.